Electronic Supplementary Material (ESI) for Materials Horizons.

3D Grape String-like Heterostructure Enable High-efficiency sodium ion capture in $Ti_3C_2T_x$ MXene/Fungi-Derived Carbon Nanoribbons Hybrids

Ningning Liu[1§], Jianhua Yuan[1§], Xiaochen Zhang[1], Yifan Ren[1], Fei Yu[3], Jie Ma[1,2*]

1 Research Center for Environmental Functional Materials, State Key Laboratory of Pollution Control and Resource Reuse, College of Environmental Science and Engineering, Tongji University, 1239 Siping Road, Shanghai 200092, P.R. China

2 School of Civil Engineering, Kashi University, Kashi 844000, China

3 College of Marine Ecology and Environment, Shanghai Ocean University, Shanghai 201306, P.R. China

§ Ningning Liu and Jianhua Yuan contributed equally to this work.

1. Materials and methods

1.1. Materials

Ti_3AlC_2 MAX powder (400 mesh) was bought from 11 Technology Co., Ltd., China. Other chemicals were purchased from Aladdin Reagent, China. Before used, the styrene monomer needed to be washed with 10 wt% NaOH aqueous solution for four times, and then deionized water was used to remove the extra NaOH until the pH of solution got neutral. Other chemicals were applied without further purification. Deionized water used in the experiments was produced by ultrapure water system.

1.2. Synthesis of MXene ($Ti_3C_2T_x$) nanosheets

The $Ti_3C_2T_x$ MXene was obtained by selective etching Al layer of the Ti_3AlC_2 precursor (400 mesh). Briefly, 2 g of lithium fluoride (LiF, >99%) was dissolved in 40 mL 9 M HCl aqueous solution in a PTFE container. The mixture was stirred for 30 min to dissolve the salt. Then 2 g of Ti_3AlC_2 powder was added into the mixture over the course of 10 min to avoid overheating of the solution as a result of the reaction's exothermic nature. The mixture was stirred for 24 h at 35 ℃, after which the suspension was repeatedly centrifuged at 3500 rpm and cleaned with deionized water a until the pH of the supernatant was more than 5. The obtained solid residue was multi-layered $Ti_3C_2T_x$. For intercalation, disperse the multi-layered $Ti_3C_2T_x$ into ethanol (≥ 99.5%) and ultrasonicate the mixture for 1h under the protection of argon gas flow. Then, the mixture was centrifuged for 10 min at 10000 rpm to collect the precipitate, which was intercalated $Ti_3C_2T_x$. For delamination, the precipitate was then added to deionized water and sonicated for 20 min in a flowing Ar atmosphere. The solution was centrifuged at 3500 rpm for 3 min to obtain a black supernatant which was Monolayered or few-layered $Ti_3C_2T_x$ suspension. To avoid the large size of MXene sheets bridged two or more PS microspheres, cell disruption was used to breakage the MXene sheets for 10 min.

1.3. Electrostatic Self-Assembly of MXene@PS nanospheres hybrids

Positively charged PS microspheres with a diameter of 570 nm were synthesized *via* a dispersion polymerization method with dimethylaminomethacrylate methyl chloride (DMC) as both cationic stabilizer and comonomer, a typical process was as follows: 13.6 g of styrene monomer, 0.272 g of azobisisobutyronitrile (AIBN), and 0.272 g of DMC were added into methanol solution (30 mL DI water/120 mL methanol) in a three-necked 250 mL round-bottomed flask in an oil bath.

The mixture was stirred at 350 rpm with argon gas protection for 30 min, and then heated to trigger the polymerization under constant stirring at 70 ℃ for 8 h. and the synthesized PS microspheres were then centrifuged and washed by methanol and DI water successively for three times. Finally, the obtained positively charged PS microspheres were dried and dispersed in DI water for further use.

The MXene@PS nanospheres hybrids were synthesized driven by electrostatic interaction between positively charged PS microspheres and negatively charged $Ti_3C_2T_x$ nanosheets. The mass ratio of $Ti_3C_2T_x$ to PS was controlled at 1: 10. First, half the mass of $Ti_3C_2T_x$ colloidal suspension (2 mg mL^{-1}) was added into the PS nanospheres suspension (10 mg mL^{-1}) and stirred for 10 min. The mixture was centrifuged for 3 min at 3500 rpm to collect the sediment. To facilitate the $Ti_3C_2T_x$ assembly on the PS nanospheres, the collected sediment was embellished with poly (diallyldimethylammonium chloride) (PDDA, 0.5 wt%) solution to endow the surface of the substrate with positive charges. After stirring for 2 hours under room temperature, the modified MXene@PS nanospheres hybrids were washed thoroughly, and re-dispersed in water. Then the other half of $Ti_3C_2T_x$ colloidal suspension (2 mg mL^{-1}) was added into the mixture under stirring. The resulting MXene@PS sediment was centrifuged and washed for 3 times. The precipitate dispersed in DI water and the MXene@PS nanospheres hybrids suspension obtained for later use.

1.4. Microbial strain culture

Aspergillus niger was cultivated by oscillating culture. The nutrient solution possessing 10 g glucose, 8 g peptone and 500 mL DI water was sterilized in an autoclave sterilizer at 121 °C for 1 h and was cooled down to room temperature. The spores of *Aspergillus niger* (ANR) were then added into the nutrient solution and cultured in a thermostatic oscillation incubator for 3 days at 35 ℃.

1.5. Coupling with MXene@PS nanospheres

The *Aspergillus niger* spheres were cleaned with DI water repeatedly until the color of washing water changed from yellow-brown to transparent. Briefly, dissolve the *Aspergillus niger* spheres hydrogels into the MXene@PS nanospheres hybrids suspension and keep an uninterrupted shaking in the oscillation incubator for 36 h at 25 ℃ for sufficient bio-adsorption process.

1.6. Hybrid MXene@PS /Microbial Sphere Aerogels

A 3D grape string-like $Ti_3C_2T_x$ MXene hollow microspheres on nitrogen-doped carbon nanoribbons (N-CNRis) heterostructures were obtained (GMNC) was acquired by vacuum freeze-

drying at -60 ℃ for 72 h, followed by an annealing process at 500 ℃ for 2 h in argon atmosphere at a heating rate of 2 °C min^{-1}. The microbial sphere aerogel transformed to N-CNRis with no biological activity, and the PS spheres were removed by thermal evaporation. $Ti_3C_2T_x$ MXene hollow microspheres (MHM) could be gained *via* directly freeze-drying and thermal treatment the MXene@PS.

1.7. CDI Electrode Materials preparation

For electrochemical test and desalination process, the electrodes were synthesized by mixing the as-prepared samples, carbon black, and polyvinylidene fluoride (PVDF) in nmethyl-2-pyrrolidone (NMP) solvent at the weight ratio of 80%: 10%: 10% to form a mixture. The obtained solid-liquid mixture was stirred magnetically for at least 12 h to produce a homogeneous slurry. Next, a doctor-blade was used to paste the slurry onto the carbon paper to prepare the electrodes with a thickness of 25 μm and a coating surface area of ~4.5×5 cm^2. After vacuum drying at 60 °C for 12 h, the electrodes were weighted and used for electrochemical measurement and desalination.

1.8. Material Characterization

Morphology and microstructures of the prepared samples were investigated by scanning electron microscopy (SEM, ZEISS Gemini 300) combined with energy-dispersive X-ray spectroscopy (EDS) element mapping analysis and transmission electron microscopy (TEM, JEOL 2010F). Dynamic light scattering (DLS) test using the Malvern Nano-ZS Zetasizer was applied for the measurement of particle size of the PS sphere. Thermogravimetric analysis (TGA, TA-SDTQ 600) was performed during the temperature range of 0 – 1000°C in a nitrogen atmosphere at a heating rate of 10°C min^{-1}. The specific surface area and pore size distribution of the prepared samples were explored by Nitrogen sorption test using a Belsorp Mini-II instrument (Japan) at 77 K. Crystal structure characteristics of materials was studied by X-ray diffraction (XRD, D8 Advance, Bruker AXS) with Cu-Kα radiation (45 kV, 40 mA) at a scan rate of 2 ℃ min^{-1}. Raman spectroscopic measurement (Renishaw inVia, 532 nm excitation) was used to describe the phase component and the degree of graphitization. X-ray photoelectron spectroscopy (XPS) reflecting the surface chemical information of materials was examined on a ThermoFisher ESCALAB 250Xi spectrometer utilizing Al-Kα radiation (1486.6 eV) with a base pressure of 1×10^9 torr. Fourier-transform infrared (FTIR) spectra test was carried out to identify the functional groups of samples.

FTIR spectra were recorded on a NEXUS 670FTIR spectrometer using KBr disks.

Surface chemistry of GMNC was evaluated using the alkalimetric–acidimetric titration method. Prepared GMNC was first dispersed in 1.0 mM NaCl solution at a solid/liquid ratio of 1 g/L. The mixtures were set for 1 weeks to allow the full hydration of surface hydroxyl groups. At the end of conditioning, the mixtures were bubbled with N_2 gas for 30 min to remove interference from the dissolved CO_2 and then titrated with 0.01 M HCl/NaOH. Alkalimetric–acidimetric titration experiments were carried out using an Metrohm 842 Titrando system, coupled with GK2401 composite glass electrode. The surface charge/surface charge density, Q, was calculated by the following equation [1, 2]:

$$Q = \frac{(C_b - C_a + [H^+] - [OH^-])}{a} \quad (1)$$

Where C_b and C_a are the concentration (mol L^{-1}) of the NaOH/HCl added, a is the concentration of solid (g L^{-1}), Q is the mean surface charge (mol Kg^{-1}), $[H^+]$ and $[OH^-]$ are derived from the recorded pH.

1.9. Electrochemical Characterization

A traditional three-electrode cell with a glassy carbon (the diameter of glassy carbon is 3 mm), Ag/AgCl and Pt wire as the working electrode (WE), reference electrode (RE) and counter electrode (CE) respectively immersing in 1M NaCl aqueous solution was employed in electrochemical measurement.

The working electrode with a mass load of 0.0588 mg. EIS measurement was operated over a frequency range from 10^5 to 10^{-2} Hz with an amplitude of 5 mV. Cyclic voltammetry (CV), galvanostatic charging/discharging cycling (GCD), and electrochemical impedance spectra (EIS) were tested using the electrochemical station (CHI660D, China.). The special capacitance (C) obtained from CV curve and GCD curve was calculated according to equation (2) and equation (3) respectively.

$$q = \frac{\int I \times dt}{m \times v \times \Delta V} \quad (2)$$

$$q = \frac{I \times \Delta t}{m \times \Delta V} \quad (3)$$

Where q represents the specific capacitance (F g^{-1}), I refers to the current (A), v is the scan rate (V s^{-1}), ΔV is the potential window (V), m corresponds the electrode material mass (g), Δt is the

discharge time (s).

The current contributions are composed of the surface-controlled and diffusion-controlled charge storage, which can be stated as follows:

$$i = av^b \quad (4)$$

$$\log\ (i) = blog\ (v) + log(a) \quad (5)$$

Where *i* and *v* represent the peak current (A) and scan rate (V s^{-1}), respectively; *a* and *b* are flexible parameters. Particularly, the *b*-value is obtained from the slope of the plot of log (*i*) versus log (*v*). If the *b*-value is 0.5, the capacity storage mainly depends on the diffusion-controlled process, otherwise the capacitive-dominated storage leads to the *b*-value close to 1.0.

The percentage of the capacitive contribution and diffusion contribution are quantified according to Dunn's method [3]:

$$i = k_1 v + k_2 v^{1/2} \quad (6)$$

Where k_1 is the (pseudo)-capacitive contribution and k_2 represents the battery-like diffusion contribution. By plotting the relationship between i/$v^{1/2}$ and $v^{1/2}$, k_1 and k_2 can be calculated from slope and y-intercept points, respectively.

The capacity contribution can be divided into the outer and inner surface-controlled capacity. The outer surface refers to the region touching the electrolyte directly, estimated from the outer charge ($q_{s,out}$); the inner surface is the region where electrolyte difficultly accesses, obtained from the inner charge ($q_{s,in}$). $q_{s,out}$ is independent of sweep rates, while the $q_{s,in}$ is a diffusion-controlled process. The detailed calculation formula is as follows:

$$q^* = q_\infty + Av^{-1/2} \quad (7)$$

$$q^{*-1} = q_s^{-1} + A_2 v^{1/2} \quad (8)$$

Where q^* is the voltammetric charge, *v* is the scan rate, A is a constant, and q_∞ is the specific capacitance at a high sweep rate (v → ∞) equaling to $q_{s,out}$. $q_{s,in}$ can be calculated from the difference between q_s and $q_{s,out}$.

In situ electrochemical quartz crystal microbalance with dissipation monitoring (EQCM-D,Qsense Analyzer, China) equipped the AT-cut quartz crystal resonator coated with a gold disk electrode with an active surface area of 0.79 cm^2 operated at a fundamental frequency of 5.0 MHz.

To prepare the spray used in EQCM-D, the active material (GMNC), acetylene black, and PVDF were dispersed in the NMP solvent in a mass ratio of 8:1:1. The RE and CE were KCl-saturated Ag/AgCl and Pt, respectively; and 10 mM NaCl solution was used as electrolyte in the EQCM-D measurement system. The quality variation (Δm, ng) of the electrodes was reflected by the change of frequency and was given by the Sauerbrey equation, as show in following:

$$\Delta m = - C_f \Delta f / n \tag{9}$$

Where C_f represents the mass sensitivity constant (17.7 ng cm^{-1} Hz^{-1} for 5 MHz crystals), Δf is the measured frequency change (Hz), n refers to the overtone number (1,3…n). The charge storage is calculated from the CV curves, as following equation,

$$\Delta Q = \int I \times dt \tag{10}$$

Where I is the instantaneous current and t is the time in a CV scan.

The theoretical mass change Δm_T (g) was calculated by Equation 11-13:

$$n(Na^+) = \frac{Q \times 6.24 \times 10^{18}}{N_A} \tag{11}$$

$$\Delta m_T = 22 \times N_A \tag{12}$$

$$n(H_2O) = \frac{\Delta m - \Delta m_T}{18} \tag{13}$$

Where $n(Na^+)$ is the molar mass of Na^+ (mol), N_A is Avogadro's constant (6.02 × 10^{23} mol), $n(H_2O)$ the molar mass of H_2O associated with Na^+.

1.10. Batch mode CDI experiments

A flow-by CDI cell was composed of a pair of acrylic plates, electrodes, rubber gaskets, and cation/anion exchange membranes, and a spacer with a volume of 0.1 × 4.5 × 5 cm^3. During the CDI process, LAND battery testing system (CT2001D) was served for power supply. NaCl solution (20 mL) was serially pumped into the CDI cell by a peristaltic pump from a tank and the effluent was returned to the tank. The deionization process was operated in constant voltage and batch mode. The flow rate sustained at 20 mL min^{-1}, and the concentration of NaCl solution was instantaneous recorded using the ion conductivity meter (Mettler Toledo S230). During the testing sessions, physicochemical adsorption equilibrium was first reached without charge, then a constant voltage was applied to realize ion electrosorption, after which the desorption of ions and regeneration of electrodes were achieved by applying a reverse voltage. Different operation voltages and various

NaCl concentration was applied to discuss the deionization performance.

The gravimetric salt adsorption capacity (SAC, mg/g) was calculated according to the equation (14):

$$SAC = \frac{(C_0 - C_e) \times V}{m} \quad (14)$$

Where C_0 and C_e (mg L^{-1}) are the concentration of NaCl at initial and final stages, respectively; V (L) is the volume of NaCl solution; and m (g) is the total mass loading of active material in working electrode.

The salt adsorption rate (SAR, mg g^{-1} min^{-1}) was acquired from the equation (15).

$$SAR = \frac{SAC}{t} \quad (15)$$

Where SAC ($mg \cdot g^{-1}$) is the desalination capacity, t is the desalination time (min).

Charge efficiency (Λ) was quantitatively determined according to equation (16)

$$\Lambda = \frac{\Gamma \times F}{\Sigma} \quad (16)$$

Where F (C mol^{-1}), Γ (mol g^{-1}), and Σ (C g^{-1}) depicted Faraday constant (96485 C mol^{-1}), salt adsorption capacity, and charge density, respectively.

The energy-normalized adsorbed salt (ENAS, mg_{NaCl} J^{-1}) was obtained based on the following equation:

$$ENAS = \frac{SAC \times m}{E_{in}} = \frac{SAC \times m}{V\int_0^t Idt} \quad (17)$$

Where E_{in}, V, t and I represents energy input during charging (J), applied voltage (V), charging time (s), and current (A), respectively.

The specific energy consumption (SEC, kJ mol^{-1}) was calculated as follows:

$$SEC = \frac{M_{NaCl}}{ENAS} \quad (18)$$

Where M_{NaCl} is the molar mass of NaCl (58.5 g mol^{-1}).

1.11 Computational details

In this work, we use the density functional theory (DFT) as implemented in the Vienna Ab initio simulation package (VASP) in all calculations. The exchange-correlation potential is described by using the generalized gradient approximation of Perdew-Burke-Ernzerhof (GGA-PBE). The projector augmented-wave (PAW) method is employed to treat interactions between ion cores and valence electrons. The plane-wave cutoff energy was fixed to 500 eV. Given structural

models were relaxed until the Hellmann–Feynman forces smaller than -0.02 eV/Å and the change in energy smaller than 10-5 eV was attained. During the relaxation, the Brillouin zone was represented by a Γ centered k-point grid of 3×3×1. A vacuum layer of around 30 Å was added in the direction perpendicular to the surface to eliminate the spurious interlayer interaction.

1.12 Finite-element simulations

Fick's second law was used to simulate the calculation domain and calculated the diffusion flux density (dimension number of ions per unit area per unit time transport through the electrodes) to evaluate the internal ion transport rate of the electrode. Fick's second law is as follows:

$$\frac{\partial C_0}{\partial t} = D_0 \nabla^2 C_0 \qquad (19)$$

In which C_0 represents the concentration of dimensions, t represents the time, D_0 represents the diffusion coefficient in dimensions. We assume that the calculation domain is filled with a certain concentration gradient of NaCl solution. We provide the salt concentration of the model at the inlet is 4.2 mol m^{-3}. The temperature was set to 25 °C, and the diffusion rate of NaCl was 2.03×10^{-9} m^2 s^{-1} [4, 5]

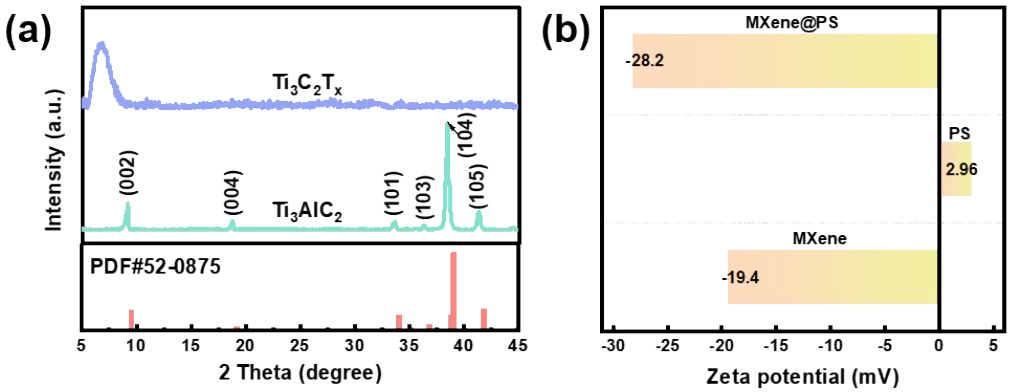

Figure S1 (a) XRD patterns of Ti_3AlC_2 and $Ti_3C_2T_x$ MXene sheet. (b) Zeta potentials of positively charged PS microspheres and negatively charged $Ti_3C_2T_x$ nanosheets

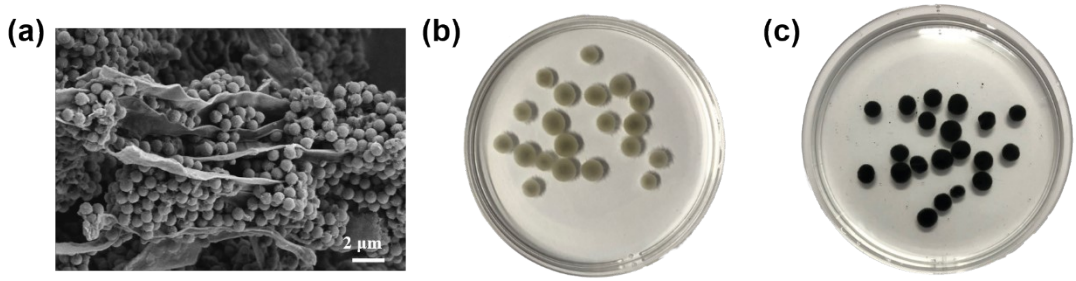

Figure S2 (a) SEM images with low magnification of $Ti_3C_2T_x$ MXene@PS/ANR hybrids; optical images of ANR (a) before and (b) after MXene adsorption

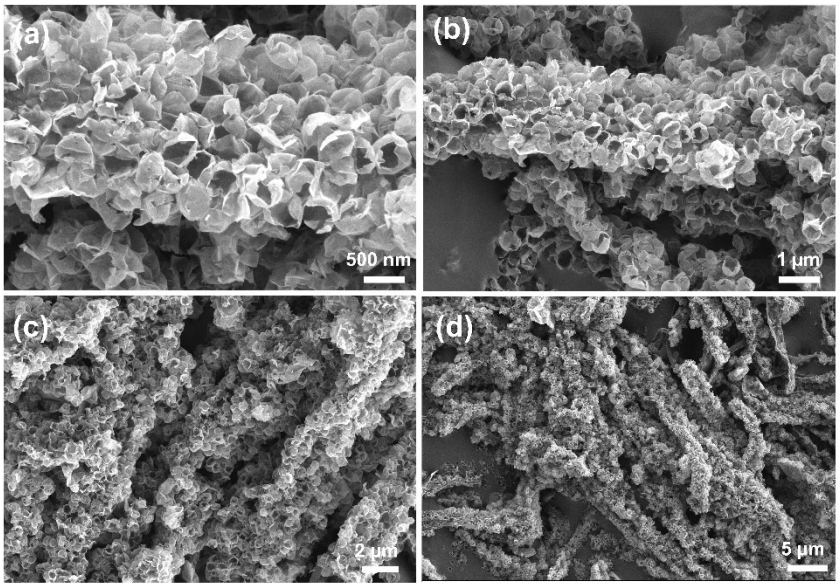

Figure S3 SEM images of GMNC at different scales

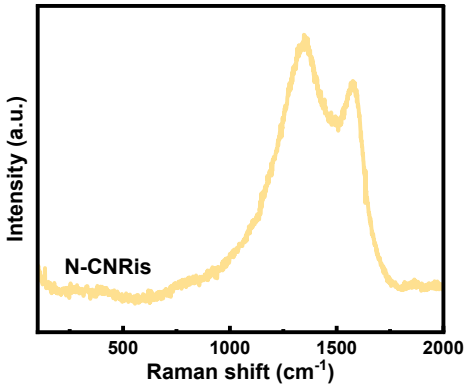

Figure S4 Raman shift of N-CNRis.

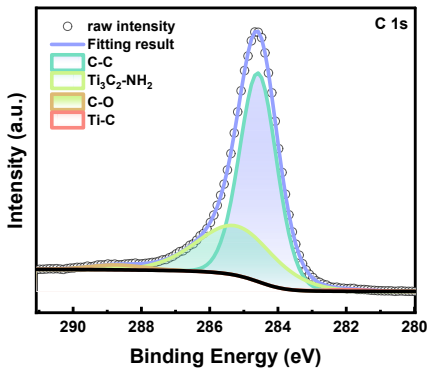

Figure S5 High-resolution XPS spectra of C 1s of GMNC.

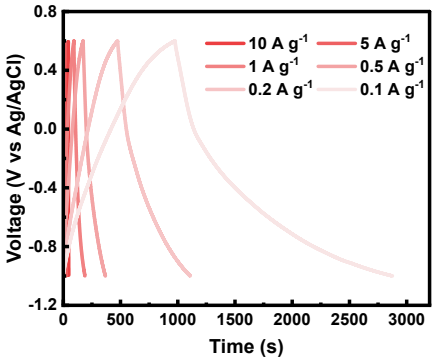

Figure S6 GCD curves of GMNC at different current density.

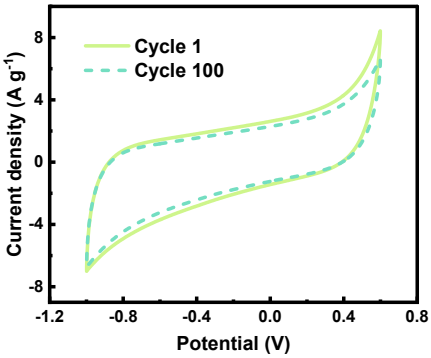

Figure S7 100 cyclic voltammetry cycling curves of GMNC at 100 mV s^{-1}.

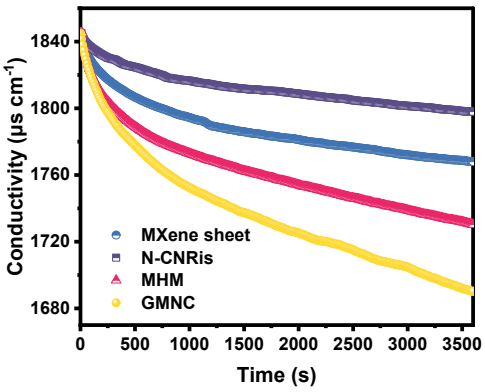

Figure S8 Conductivity variations of $Ti_3C_2T_x$ MXene sheet, N-CNRis, MHM, and GMNC in 1000 mg L^{-1} NaCl concentration and applied voltage is 1.2 V.

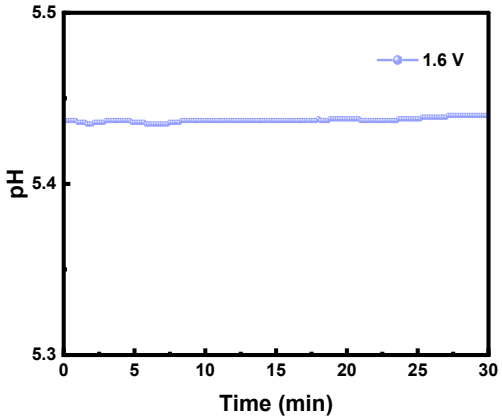

Figure S9 pH value during the adsorption process.

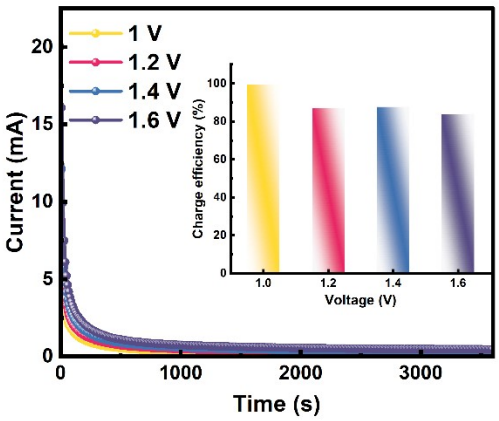

Figure S10 Current vs. time of GMNC and the corresponding charge efficiency at various operation voltages in 1000 mg L^{-1} NaCl solution.

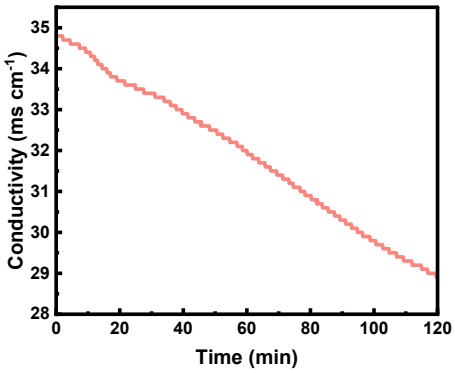

Figure S11 Solution conductivity vs. runtime of GMNC electrode in a NaCl aqueous solution of 500 mM upon an external voltage of 1.6 V for 120 min.

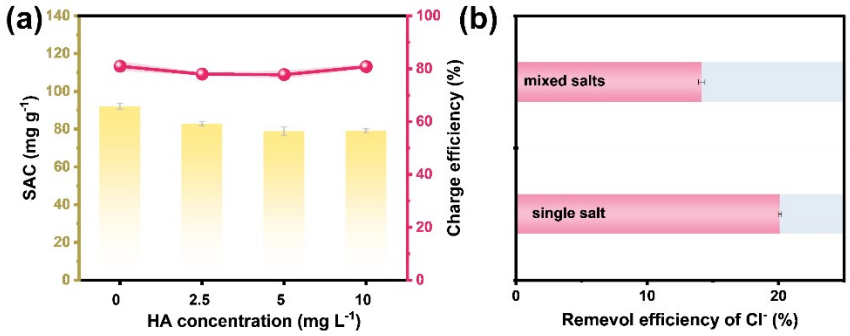

Figure S12 (a) The salt adsorption capacity and charge efficiency of GMNC in the presence of different HA concentrations in 10 mM NaCl solution at 1.2 V charging for 60 min. (b) Chloride ion removal performance in the presence of foreign anion at 1.2 V charging for 60 min.

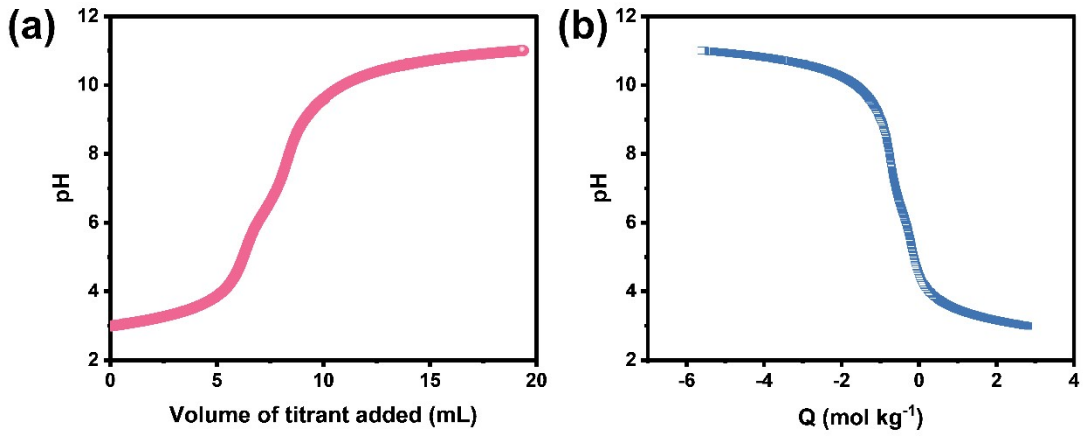

Figure S13 (a) Representation of alkalimetric titration and (b) surface charge (Q) curve of GMNC in 1 mM NaCl solution.

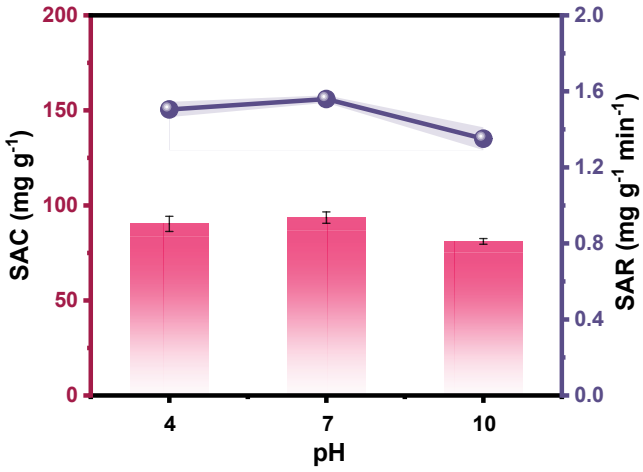

Figure S14 SAC and SAR variations of GMNC in 1000 mg L^{-1} NaCl solution at 1.2 V for 60 min

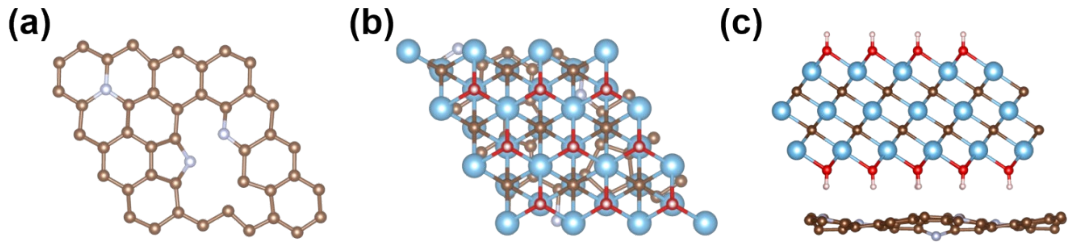

Figure S15 Schematic diagram showing the optimized crystal structure of (a) N-CNRis, (b) the top view and (c) side view of GMNC. The blue, brown, red, pink and white balls represent Ti, C, O, H, and N atoms, respectively.

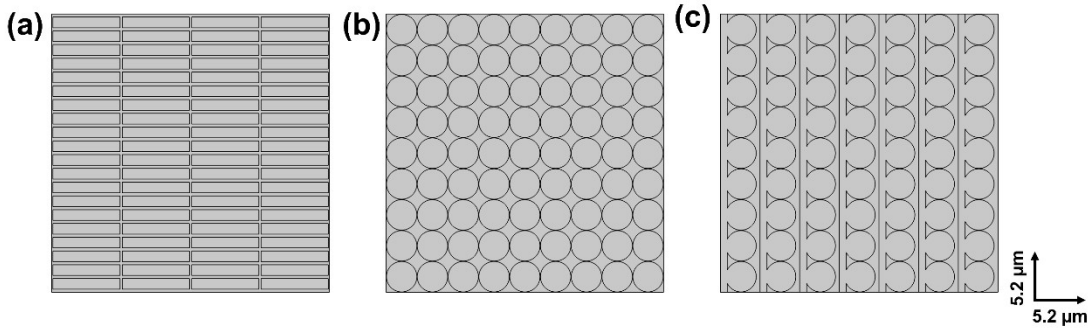

Figure S16 The electrode models built in COMSOL Multiphysics software for (a) MXene sheet, (b) MHM, and (c) GMNC.

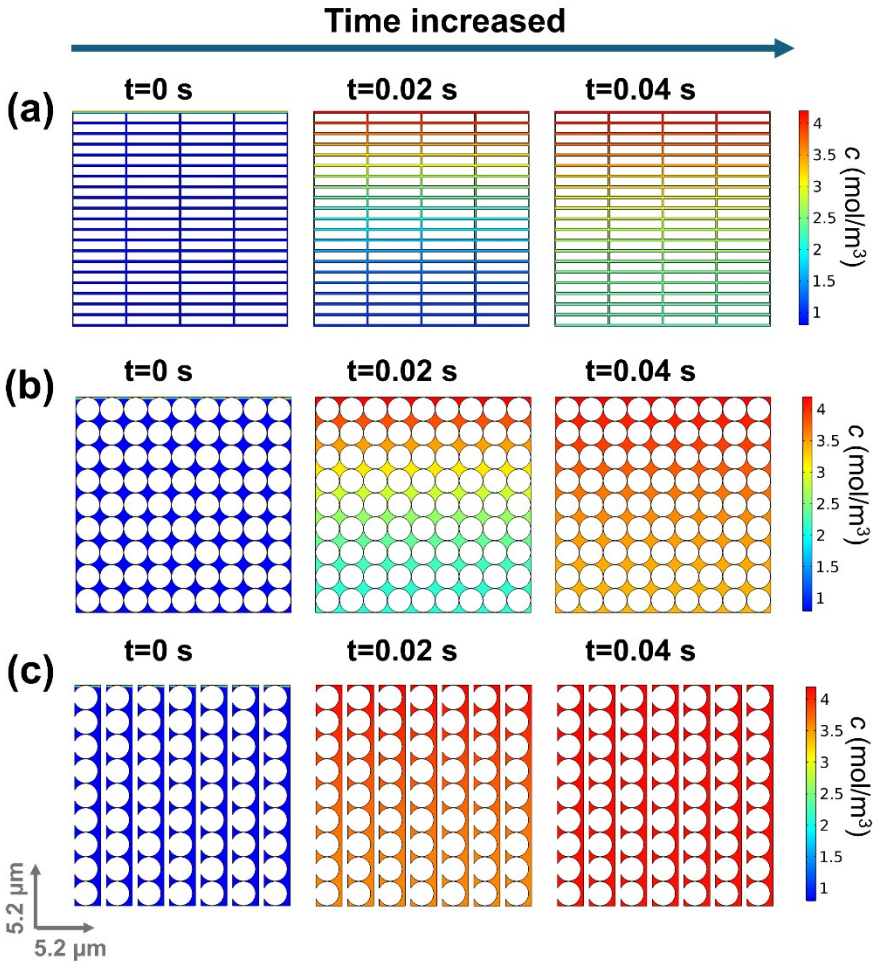

Figure S17 Finite element simulation results for the constant concentration vacations in 2D models with time (0−0.04 s): (a) MXene sheet, (b) MHM, and (c) GMNC.

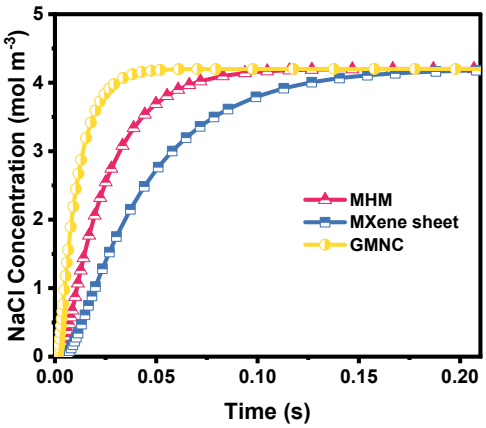

Figure S18 The NaCl concentration change versus time in MXene sheet, MHM, and GMNC models.

Table S1 Comparation of the CDI performance of in the state-of-the-art MXene-based materials with GMNC

MXene-based electrode	**Initial salt concentration (mg L^{-1})**	**Applied voltage**	**Desalination capacity (mg g^{-1})**	**Desalination Rate (mg g^{-1} min^{-1})**	**Long term stability**	**Ref.**
$Ti_3C_2T_x$	292.5	1.2 V	13	0.43	40	[6]
CLF@$Ti_3C_2T_x$	600	1.2V	35	0.58	10	[7]
bi-stacked $Ti_3C_2T_x$	877.5	1.2 V	39	2.6	25	[8]
MXene/CNT	500	1.2 V	34.5	1.035	40	[9]
$W_{18}O_{49}/Ti_3C_2$	500	1.2 V	29.25	0.975	10	[10]
MoS_2@MXene	500	1.2 V	35.6	2.6	40	[11]
$TiO_2/Ti_3C_2T_x$	1500	1.2 V	23.8	0.39	20	[12]
NaOH-$Ti_3C_2T_x$	100	1.2 V	12.19	-	20	[13]
MXene/BC	585	1.2 V	12.27	1.23	20	[14]
PPy-NiCo-LDH@MXene	200	1.2 V	31.5	4.7	40	[15]
MXene@COF	500	1.2 V	24.5	0.81	100	[16]
Fe_3O_4@Ti_3C_2	500	1.2 V	44	1.47	40	[17]
mPDA/MXene	1000	1.5 V	37.72	1.27	200	[18]
N–$Ti_3C_2T_x$	5000	1.2 V	43.5±1.7	-	24	[19]
Functionalized MXene	5000	1.2 V	49	2.92	100	[20]
1D TiO_2/2D Ti_3C_2	500	1.2 V	64.32	1.07	40	[21]
GMNC	1000	1.2 V	107.38	1.78	100	This work
	1000	1.6 V	162.37	2.71	-	This work

Table S2 Comparation of the energy consumption of in the state-of-the-art CDI electrode materials with GMNC

CDI electrode	**Applied voltage/specific current**	**Energy consumption (KJ mol^{-1})**	**Ref.**
mPDA/MXene//AC	1.5 V	162.48	[18]
PB/PANI//AC	100 mA g^{-1}	212.71	[22]
Na-FeOOH//Cl-FeOOH	1.2 V	185.00	[23]
$FePO_4$@RGO//RGO	1.8V	190.00	[24]
NiHCF@3DC-2 // AC	0.8 V	93.5	[25]
GMNC//AC	1.0 V	95.25	This work

Table S3. The values of $\triangle m_1$, $\triangle m_2$, $n(Na^+)$ and $n(H_2O)$ during the Na^+ absorption process

Current density (mA g^{-1})	**Q (mC)**	**$\triangle m$ (ng)**	**$\triangle m_t$ (ng)**	**$N(Na^+)$ (nmol)**	**$N(H_2O)$ (nmol)**
0	0.830	277.29	189.20	8.60	4.89

1. A. Hemmatifar, D. I. Oyarzun, J. W. Palko, S. A. Hawks, M. Stadermann and J. G. Santiago, *Water Research*, 2017, **122**, 387-397.
2. S. Xu, S.-P. Li, T. Wang and C.-F. Wang, *Langmuir*, 2019, **35**, 628-640.
3. D. Chao, P. Liang, Z. Chen, L. Bai, H. Shen, X. Liu, X. Xia, Y. Zhao, S. V. Savilov, J. Lin and Z. X. Shen, *ACS Nano*, 2016, **10**, 10211-10219.
4. M. Liu, Y. Pang, B. Zhang, P. De Luna, O. Voznyy, J. Xu, X. Zheng, C. T. Dinh, F. Fan, C. Cao, F. P. G. de Arquer, T. S. Safaei, A. Mepham, A. Klinkova, E. Kumacheva, T. Filleter, D. Sinton, S. O. Kelley and E. H. Sargent, *Nature*, 2016, **537**, 382-386.
5. X. Liu, X. Xu, X. Xuan, W. Xia, G. Feng, S. Zhang, Z.-G. Wu, B. Zhong, X. Guo, K. Xie and Y. Yamauchi, *Journal of the American Chemical Society*, 2023, **145**, 9242-9253.
6. P. Srimuk, F. Kaasik, B. Krüner, A. Tolosa, S. Fleischmann, N. Jäckel, M. C. Tekeli, M. Aslan, M. E. Suss and V. Presser, *Journal of Materials Chemistry A*, 2016, **4**, 18265-18271.
7. S. Anwer, D. H. Anjum, S. Luo, Y. Abbas, B. Li, S. Iqbal and K. Liao, *Chemical Engineering Journal*, 2021, **406**, 126827.
8. S. Buczek, M. Barsoum, S. Uzun, N. Kurra and Y. Gogotsi, *Energy & Environmental Materials*, 2020.
9. Y. Cai, L. Zhang, R. Fang, Y. Wang and J. Wang, *Separation and Purification Technology*, 2022, **292**, 121019.
10. J. Liang, J. Yu, W. Xing, W. Tang, N. Tang and J. Guo, *Chemical Engineering Journal*, 2022, **435**, 134922.
11. Y. Cai, Y. Wang, L. Zhang, R. Fang and J. Wang, *ACS Applied Materials & Interfaces*, 2022, **14**, 2833-2847.
12. W. XI and H. LI, *Journal of Inorganic Materials*, 2021, **36**, 283-291.
13. B. Chen, A. Feng, R. Deng, K. Liu, Y. Yu and L. Song, *ACS Applied Materials & Interfaces*, 2020, **12**, 13750-13758.
14. B. Li, K. Sun, W. Xu, X. Liu, A. Wang, S. Boles, B. Xu, H. Hu and D. Yao, *Nano Research*, 2022, DOI: 10.1007/s12274-022-4491-3.
15. Y. Cai, Y. Wang, R. Fang and J. Wang, *Separation and Purification Technology*, 2022, **280**, 119828.
16. S. Zhang, X. Xu, X. Liu, Q. Yang, N. Shang, X. Zhao, X. Zang, C. Wang, Z. Wang and J. G. Shapter, *Materials Horizons*, 2022, **9**, 1708-1716.
17. K. Wang, L. Chen, G. Zhu, X. Xu, L. Wan, T. Lu and L. Pan, *Desalination*, 2022, **522**, 115420.
18. Q. Li, X. Xu, J. Guo, J. P. Hill, H. Xu, L. Xiang, C. Li, Y. Yamauchi and Y. Mai, *Angewandte Chemie International Edition*, 2021, **60**, 26528-26534.
19. A. Amiri, Y. Chen, C. Bee Teng and M. Naraghi, *Energy Storage Materials*, 2020, **25**, 731-739.
20. Z. Bo, Z. Huang, C. Xu, Y. Chen, E. Wu, J. Yan, K. Cen, H. Yang and K. Ostrikov, *Energy Storage Materials*, 2022, **50**, 395-406.
21. N. Liu, L. Yu, B. Liu, F. Yu, L. Li, Y. Xiao, J. Yang and J. Ma, *Advanced Science*, 2023, **10**, 2204041.
22. W. Shi, X. Liu, T. Deng, S. Huang, M. Ding, X. Miao, C. Zhu, Y. Zhu, W. Liu, F. Wu, C. Gao, S.-W. Yang, H. Y. Yang, J. Shen and X. Cao, *Advanced Materials*, 2020, **32**, 1907404.
23. J. Zhao, B. Wu, X. Huang, Y. Sun, Z. Zhao, M. Ye and X. Wen, *Advanced Science*, 2022, **9**, 2201678.
24. J. Ma, L. Wang, F. Yu and X. Dai, *Chemical Engineering Journal*, 2019, **370**, 938-943.
25. S. Wang, G. Wang, Y. Wang, H. Song, S. Lv, T. Li and C. Li, *ACS Applied Materials & Interfaces*, 2020, **12**, 44049-44057.